High concentration nitrogen doped carbon nanotube anodes with superior Li+ storage performance for lithium rechargeable battery application

Xifei Li, Jian Liu, Yong Zhang, Yongliang Li, Hao Liu, Xiangbo Meng, Jinli Yang, Dongsheng Geng, Dongniu Wang, Ruying Li, Xueliang Sun*

Nanomaterials and Energy Lab, Department of Mechanical and Materials Engineering, University of Western Ontario, London, Ontario N6A 5B9, Canada

ABSTRACT

A floating catalyst chemical vapor deposition method has been developed to synthesize carbon nanotubes doped with a high concentration of nitrogen. Their electrochemical performance as anodes for lithium ion batteries (LIBs) in comparison to pristine carbon nanotubes (CNTs) has been investigated. X-ray photoelectron spectroscopy results indicated that the nitrogen content reaches as high as 16.4 at.%. Bamboo-like compartments were fabricated as shown by high resolution transmission electron microscopy. High concentration nitrogen doped carbon nanotubes (HN-CNTs) show approximately double reversible capacity of CNTs: 494 mAh g^{-1} vs. 260 mAh g^{-1}, and present a much better rate capability than CNTs. The significantly superior electrochemical performance could be related to the high electrical conductivity and the larger number of defect sites in HN-CNTs for anodes of LIBs.

© 2011 Elsevier B.V. All rights reserved.

1. Introduction

Relying upon electrical energy storage for technological applications like consumer electronics and hybrid electric vehicles (HEVs), the society progression motivates the urgent need to create high performance lithium ion batteries (LIBs). Therefore, a lot of attentions have recently been concentrated to the development of some anode materials with high specific capacities such as Si and Sn [1–3]. However, the development has not yet reached the perfection level, and some key challenges still exist in terms of improving their low electron transport at high charge–discharge rates and other aspects in poor cycle performance due to their intrinsic nature of huge lattice expansion/shrinkage causing pulverization during the charge and discharge process [4,5]. Their poor cycle performance has already been a critical hurdle hindering their applications in the large-scale LIBs [6,7]. On the other side, carbon based materials like the commercialized graphite have already been promising anodes for LIBs due to a readily available and low-cost resource as well as good cycle stability [8]. In addition to the traditional graphite and various natural and synthesized carbon based anode materials, nanostructured carbon materials have far more potential to make contributions to an increase of the specific capacities of anodes for LIBs [9–11]. Carbon nanotube (CNT)

is a hollow cylinder of pure carbon and the nanochannels within them are big enough to accommodate various atoms and even small molecules [8]. CNT can be envisioned as a rolled up graphene sheet into a seamless cylinder with fullerene caps [12]. Being one of the most representative nanostructured carbon materials, CNT presents various remarkable characteristics which include outstanding electrical properties, strong mechanical strength, greater chemical stability, higher aspect ratios, and more activated surface areas [13,14]. Following the synthesis of CNTs, they have attracted much attention for both fundamental science and applied research [15–17]. Li+ storage capacity in CNTs results from the effective diffusion of Li+ into stable sites located on the nanotube surface and inside individual nanotubes through endcap or sidewall openings as well as CNT layers [3]. Therefore, the Li+ storage in CNTs differing from the commercialized graphite anode makes CNTs to increase the stored energy density and improve the Li+ diffusion rate, being one of the most promising candidates as anodes for LIBs [18–20].

Recent works have shown that the Li+ storage behavior in CNTs employed as anodes of LIBs strongly depends on its morphology, microstructure, and synthesis method [21,22]. It was reported that carbon nanotube array on tantalum foils showed higher capacity and better cycle performance as well as rate capability than entangled carbon nanotube [22]. Maier et al. stated CNFs@CNTs displayed a twice volumetric capacity as high as that of pristine CNTs due to a higher spatial utilization [21]. Many efforts have been devoted to improving the reversible capacity of CNT anode by various alternative treatments [9,23–27], such

as single-wall carbon nanotubes (SWCNTs) employed [23], ball milling CNTs [24], binder-free in CNT anode [27] and controlling and optimizing the microstructure composition of impurity graphitic nanoparticles or graphene fragments in the matrix of the carbon nanotubes [9]. As reported by Landi et al., SWCNTs with high purity exhibited a high reversible capacity of $520 \, mAh \, g^{-1}$ [23]. However, the obtained high capacity is based on the expensive SWCNTs. It is well known that the heteroatom doping in the carbon materials is an effective approach to tailor both chemical and physical nature of carbon based anode materials [28,29]. For example, nitrogen doped carbon nanofibres are evidenced to be metallic due to the pyridine-like nitrogen and bridgehead-nitrogen type [30]. Doping heteroatoms into carbon anodes has an important influence on Li^+ storage performance for LIBs, for instance, the polymerized carbon nitride (10 at.%) nanobells improved Li^+ intercalation/de-intercalation performance with a high reversible capacity of $480 \, mAh \, g^{-1}$ [31]. Similarly, the nitrogen concentration in CNT structure could effectively impact Li^+ storage properties. The higher nitrogen doping concentration, the more significant influence of Li^+ storage performance on CNTs [32]. The rapid development in the field of CNTs, especially in the successful synthesis of nitrogen doped CNTs, provides us with a great opportunity to investigate the influence of high concentration nitrogen doped CNTs on Li^+ storage performance. Unfortunately, few research was paid attention to the high concentration nitrogen doped CNTs as anode for LIBs.

In this paper, we report the different electrochemical performance of Li^+ intercalation/de-intercalation in 16.4 at.% nitrogen doped CNTs synthesized by using a floating catalyst chemical vapor deposition (FCCVD) approach in comparison to the pristine CNTs as anodes for LIBs. It has been found that high nitrogen concentration doped carbon nanotubes (HN-CNTs) can exhibit a much higher reversible capacity and better rate capability compared with non-doped CNTs for LIBs. The mechanisms of Li^+ storage are also discussed.

2. Experimental

2.1. Synthesis of CNTs and HN-CNTs

A FCCVD method, as described in our work [33–36], was applied to synthesize CNTs and HN-CNTs based on a simple horizontal quartz tube furnace system. A quartz boat was put in the middle of the quartz tube as the substrate for the growth of CNTs and HN-CNTs. For both CNTs and HN-CNTs, 50 mg ferrocene ($Fe(C_5H_5)_2$) (98%, Aldrich) was employed as the catalyst and placed at the entrance of the furnace. 2 g imidazole ($C_3H_4N_2$) (99%, Aldrich) was used as both precursor of carbon and nitrogen for the growth of HN-CNTs. It was put beneath ferrocene at the entrance of the furnace. The ethylene gas was chose as the carbon source for the growth of CNTs. In a typical process, the argon (Ar) gas (99.999%) was introduced into the quartz tube at a flow rate of 500 sccm for 10 min in order to expel the air in the quartz tube. After that, the furnace was heated to 850 °C at a rate of 60 °C min^{-1}. To synthesize CNTs, the ethylene gas was introduced into the system at a flow rate of 15 sccm. Once the temperature reached 850 °C, the ferrocene evaporated and was carried by Ar gas into the high temperature region, where the pyrolysis and growth occurred, and CNTs were formed on the quartz boat. In the case of HN-CNTs, when the temperature reached 850 °C, the imidazole and the ferrocene evaporated simultaneously and were carried by Ar gas into the high temperature region, where the growth of HN-CNTs happened. The growth of CNTs and HN-CNTs lasted for 10 min, and then, the ethylene gas was stopped (for CNTs), the system was turned off and cooled down to room temperature in the flowing Ar gas. Both samples of CNTs and HN-CNTs were collected from the quartz boat.

2.2. Characterization of CNTs and HN-CNTs

The morphologies of CNTs (the impurity like Fe catalyst is ~5%) and HN-CNTs (the similar impurity as CNTs) were analyzed in a field emission scanning electron microscope (FE-SEM, Hitachi S-4800), transmission electron microscope (TEM, Hitachi H-7000), and high-resolution transmission electron microscope (HRTEM, JEOL 2010F). Raman spectra were obtained using a HORIBA Scientific LabRAM HR Raman spectrometer system equipped with a 532.4 nm laser as the exciting radiation equipped with an optical microscope at room temperature. X-ray photoelectron spectroscopy (XPS) analysis was carried out with a Kratos Axis Ultra Al (alpha) X-ray photoelectron spectroscopy operated at 14 kV. Powder X-ray diffraction (XRD) patterns were recorded by Rigaku RU-200BVH diffractometer employing a Co-K$_\alpha$ source ($\lambda = 1.7892$ Å). N_2 adsorption/desorption isotherms were obtained using a Folio Micromeritics TriStar II Surface Area and Pore Size Analyser.

2.3. Electrochemical storage behavior

Working electrodes were prepared by slurry casting on a Cu foil as a current collector. The slurry contained the active material (CNTs or HN-CNTs) (90 wt.% on dry solids basis) and a polyvinylidene fluoride binder (10 wt.% on dry solids basis) in N-methylpyrrolidinone (NMP) solvent. The electrodes were dried in a vacuum oven at 100 °C overnight. A coin-type half-cell consisted of a prepared electrode (~0.2 g cm^{-3} of electrode density), polypropylene separator (Celgard 2400), and lithium foil as the counter electrode. The electrolyte was composed of 1 M LiPF$_6$ salt dissolved in ethylene carbonate (EC):diethyl carbonate (DEC):ethyl methyl carbonate (EMC) in a 1:1:1 volume ratio. CR-2325-type coin cells were assembled in a glove box under a dry argon atmosphere (moisture and oxygen concentration <1 ppm). Cyclic voltammetry tests were performed on a versatile multichannel potentiostat 3/Z (VMP3) at a scan rate of 0.1 mV s^{-1} over a potential range of 0.01–3.0 V (vs. Li$^+$/Li). Charge–discharge characteristics were tested galvanostatically between 0.01 and 3.0 V (vs. Li$^+$/Li) at room temperature using an Arbin BT-2000 Battery Test System.

3. Results and discussion

3.1. Morphology of CNTs and HN-CNTs

Fig. 1 shows FE-SEM, TEM and HRTEM images of CNTs and HN-CNTs, respectively. The aligned CNTs vary from 10 to 80 nm in diameter, as shown in Fig. 1a. From the TEM image in Fig. 1b, some catalyst particles promoting the CNT growth are clearly observed inside of the CNTs. The morphology of HN-CNTs reveals straighter and smoother than the regular CNTs. The similar bond length makes nitrogen element suitable for incorporation into the CNT graphene layers. But the C–N bond length is shorter than C–C, resulting in the curving of basal planes forming the bamboo-like structure after nitrogen doping in the carbon nanotubes [34,36], as it was observed in Fig. 1d. HRTEM images can give more detailed information about the structure of CNTs and HN-CNTs. HN-CNTs display more structural defects, while CNTs have relatively higher degree of graphitization. In Fig. 1f, the curved walls of the bamboo compartment adhere perfectly to the nanotube walls, and inner nanotubes are separated into a series of bamboo-like compartments, which confirms the influence of nitrogen introduction on the structure change of CNTs.

3.2. Structure analysis of CNTs and HN-CNTs

XPS analysis was carried out in order to detect the content and bonding environment of nitrogen atoms in HN-CNTs. Fig. 2a shows
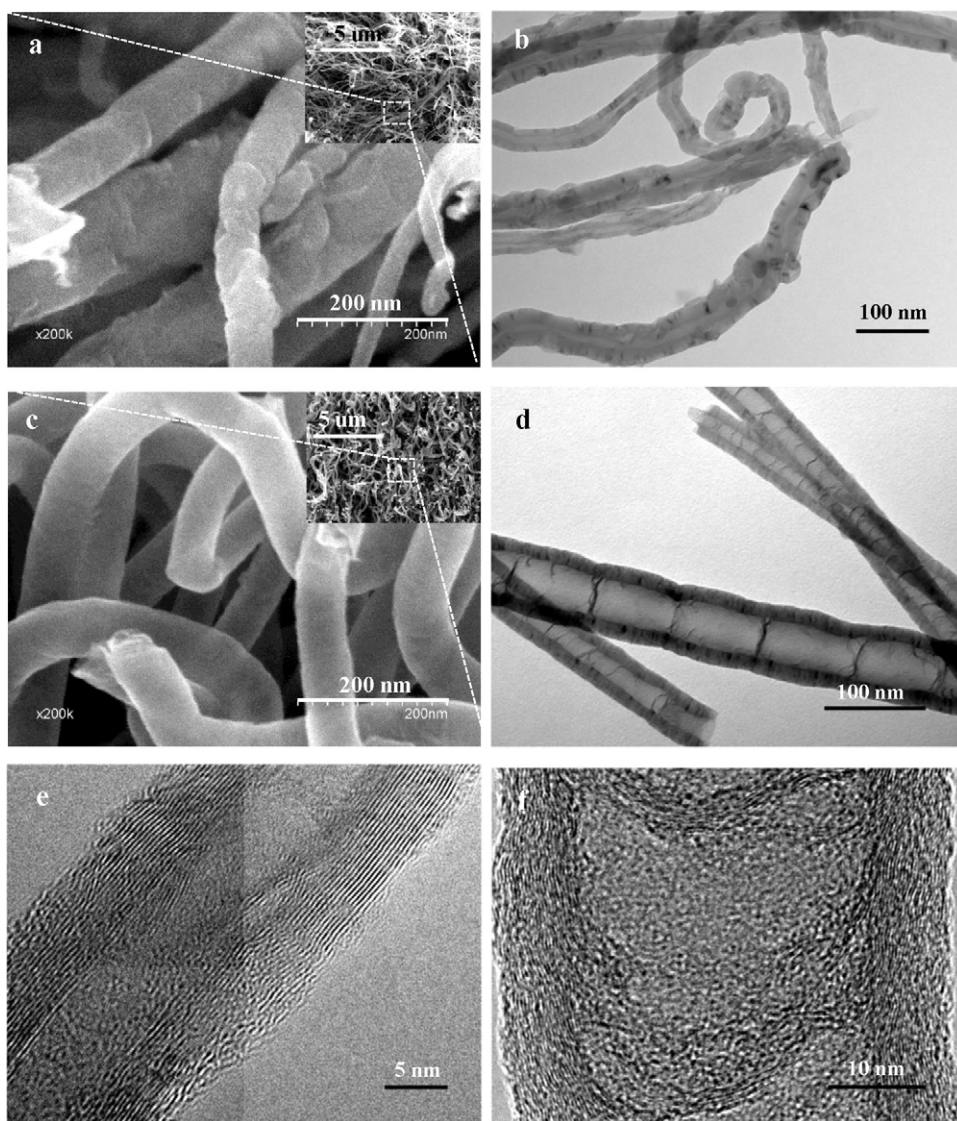
Fig. 1. SEM, TEM, and HRTEM images of (a, b and e) CNTs and (c, d and f) HN-CNTs.

a typical XPS survey scan of CNTs and HN-CNTs. The main peaks are distinguished as C1s, N1s, and O1s signals centered at 282 eV, 397 eV, and 529 eV, respectively. HN-CNTs show the distinct N1s peak, while no N1s peak for CNTs. The nitrogen content, defined as atomic percent of N with respect to the sum of C and N, is estimated by the area ratio of N peak and the sum of C and N peaks (N/(C+N)). The nitrogen content is determined to be 16.4 at.% for HN-CNTs. To get insight to the bonding environment of nitrogen in HN-CNTs, the deconvolution of N1s peak was carried out and the result is shown in Fig. 2b. The N1s spectrum of HN-CNTs consist of two distinct peaks located at 398.4 eV and 401.0 eV. During the synthesis of HN-CNTs at 850 °C, the nitrogen atoms from imidazole can incorporate into the graphene layers to replace carbon atoms at the different sites and form the different bonding between carbon and nitrogen shown various binding energies in the XPS spectra: pyridinic N (398.4 eV), and graphitic N (401.0 eV) [34,37,38]. The pyridinic nitrogen doped at the edges of the graphitic carbon layers results from the nitrogen substitution in C_6 benzene ring based on the nitrogen bonded with two sp^2 carbons. The graphitic nitrogen doped inside the graphitic carbon plane bonds with three sp^2 carbons. XPS results indicate that at 850 °C the N atoms can incorporate into the carbon structures to replace the carbon atoms located at the

edges and inside of the graphitic carbon layers forming pyridinic N and graphitic N in HN-CNTs.

XRD patterns of CNTs and HN-CNTs are shown in Fig. 3a. Both exhibit the (0 0 2) and (1 0 0) basal plane diffraction characteristic at 2θ around 30.7° and 52.1° in the hexagonal graphitic carbon structure. It can be found that the diffraction peaks of HN-CNTs slightly shifted to lower 2θ values compared with those of pristine CNTs. This shift can be attributed to the slight distortion in crystalline regularity along a or b direction by the introduction of C–N bonding shorter than C–C bonding [39,40]. Fig. 3b shows the N_2 adsorption-desorption isotherms of CNTs and HN-CNTs. Both exhibit type-I isotherm associated with the presence of micropores and mesopores [41]. The BET surface area and average pore volume for CNTs are 44.95 $m^2 g^{-1}$ and 0.081 $cm^3 g^{-1}$, while 40.92 $m^2 g^{-1}$ and 0.073 $cm^3 g^{-1}$ for HN-CNTs, respectively. They show similar pore size, ~7.3 nm.
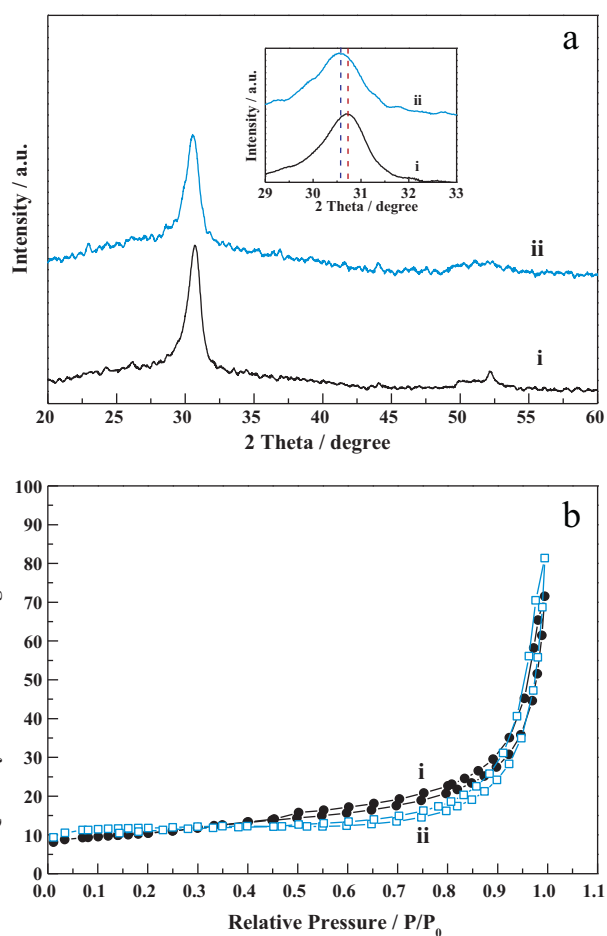
3.3. Electrochemical Impedance spectra of CNTs and HN-CNTs

The assembled cells were galvanostatically charged and discharged at a current density of 100 mA g^{-1}. The electrochemical impedance spectra (EIS) were tested at the open circuit voltage
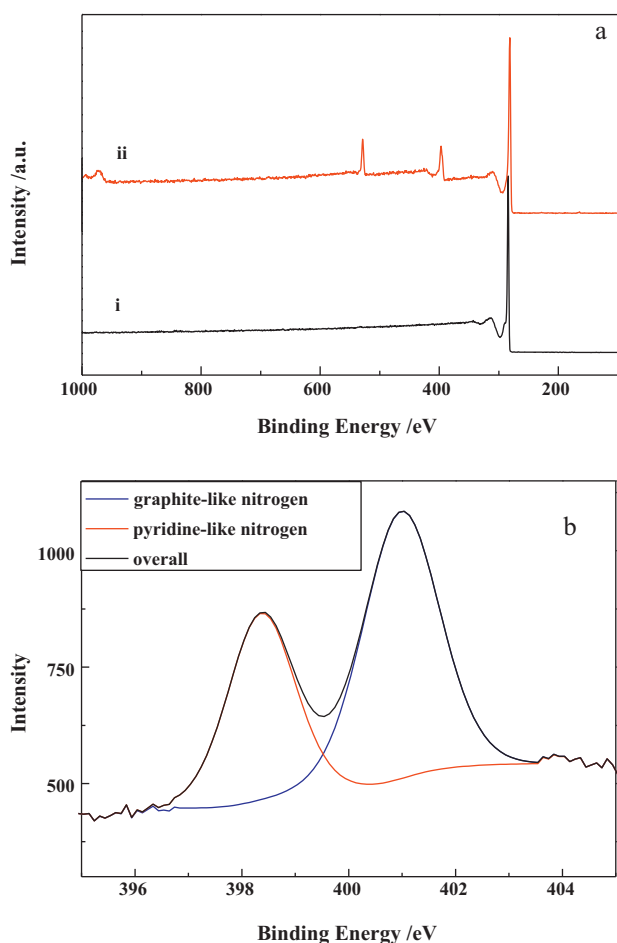
**Fig. 2.** (a) XPS full scan spectra for (i) CNTs and (ii) HN-CNTs; (b) XPS spectra of N1s in HN-CNTs.

Fig. 3. (a) XRD patterns of (i) CNTs and (ii) HN-CNTs; *inset*: XRD patterns of (i) CNTs and (ii) HN-CNTs in the range of 29–33° in Fig. 3a; (b) N_2 adsorption–desorption isotherms of (i) CNTs and (ii) HN-CNTs.

and 0.01 V of the first discharge. Fig. 4 shows EIS for CNTs and HN-CNTs, respectively. It is observed that for both anodes, there is one semicircle in the high frequency region and a line at low frequencies in the EIS tested at the open circuit voltage (see the inset in Fig. 4). However, there exist two semicircles in the high and medium frequency region in the EIS at 0.01 V. In the first discharge process, there is a close contact between anodes and electrolyte. Their interaction at some voltage results in the decomposition of electrolyte causing solid electrolyte interphase (SEI) film formation on the anodes. In comparison to the EIS at the open circuit voltage, another semicircle at 0.01 V reflects Li^+ migration through SEI. In order to simulate Li^+ intercalation into CNTs and HN-CNTs, a possible equivalent circuit is depicted in the inset of Fig. 4. R_e is the electrolyte ohmic resistance, while R_{sl} corresponds to the resistance for Li^+ migration through the SEI film and C_{sl} denotes interfacial capacitance corresponding to R_{sl}. C_{dl} and R_{ct} are the double-layer capacitance and charge transfer resistance, respectively. W is the finite length Warburg impedance that reflects the solid-state diffusion in the anodes. As it is shown in Fig. 4, the impedance value of CNTs is higher than HN-CNTs. After simulating by the equivalent circuit, it is found that the charge transfer resistance of CNTs and HN-CNTs is 58 Ω and 38 Ω, respectively. Nitrogen atom has additional lone pairs of electrons, and contributes additional electrons and provides electron carriers for the conduction band [34,42]. Thereby, HN-CNTs show higher electrical conductivity than CNTs. As a consequence, the higher electrical conductivity of HN-CNTs decreases the charge transfer resistance of anode
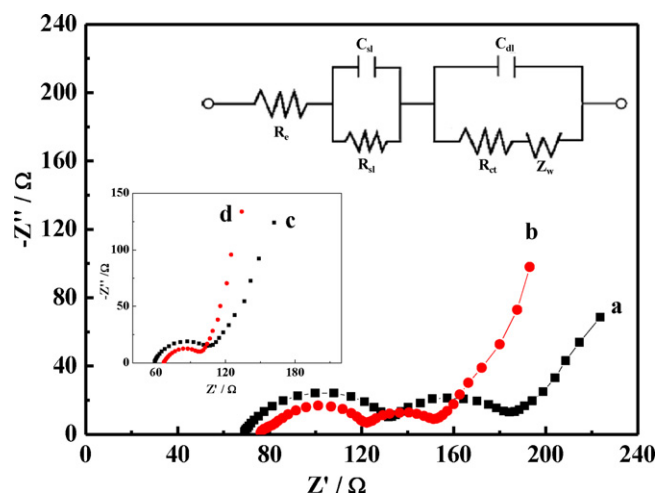
Fig. 4. Electrochemical impedance spectra of (a) CNTs and (b) HN-CNTs at 0.01 V in the first discharge; *inset*: the electrochemical impedance spectra of (c) CNTs and (d) HN-CNTs at the open circuit voltage and the equivalent circuit to fit the EIS.
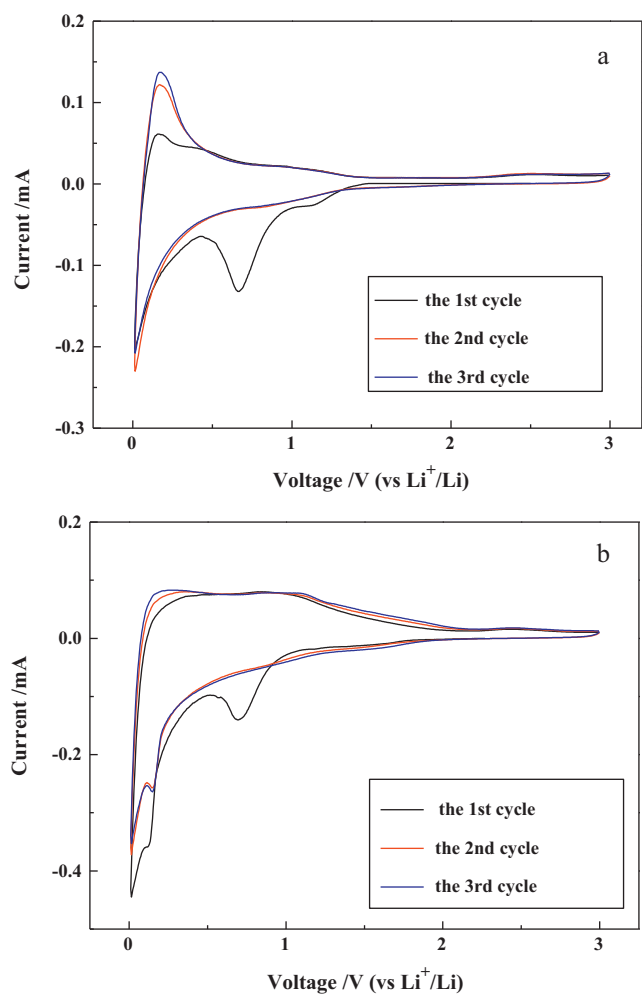
Fig. 5. Cyclic voltammograms of (a) CNTs and (b) HN-CNTs as anodes at a scan rate of 0.1 mV s^{-1} in a voltage range of 0.01–3.00 V.

materials [43–45]. This is beneficial for Li$^+$ intercalation/de-intercalation into the anodes.

3.4. Different Li$^+$ storage behavior of CNTs and HN-CNTs

The electrochemical activities of CNTs and HN-CNTs as anodes for LIBs were examined by cyclic voltammetry (CV). Fig. 5 presents the CV curves of CNT and HN-CNT anodes in the first three scanning cycles. Both CNTs and HN-CNTs show the similar CV curves. In the first cathodic scan, an obvious peak related to the decomposition of electrolyte causing SEI film formation was observed at around 0.7 V, which presumably results in the irreversible reaction for CNTs and HN-CNTs. The disappearance of this peak in the subsequent cycles indicates that the as-formed SEI film is highly stable and avoids further contact between electrolyte and anodes, which is beneficial to decrease the irreversible capacity. Another peak close to 0 V is due to the Li$^+$ intercalation into CNTs and HN-CNTs. The observed oxidation peaks located at 0.2 V show Li$^+$ de-intercalation process from anodes. It was also observed that HN-CNTs show a small peak located at 0.12 V in the first cathodic scan (shifting to 0.15 V in the sequent cycles). In comparison to CNTs, HN-CNT anode exhibits another different peak reflecting extra Li$^+$ storage sites resulting from the nitrogen doping and the forming defects, which is beneficial to increase the specific capacity.

Fig. 6a and b depict the typical galvanostatic charge and discharge curves for the CNTs and HN-CNTs at a current density of
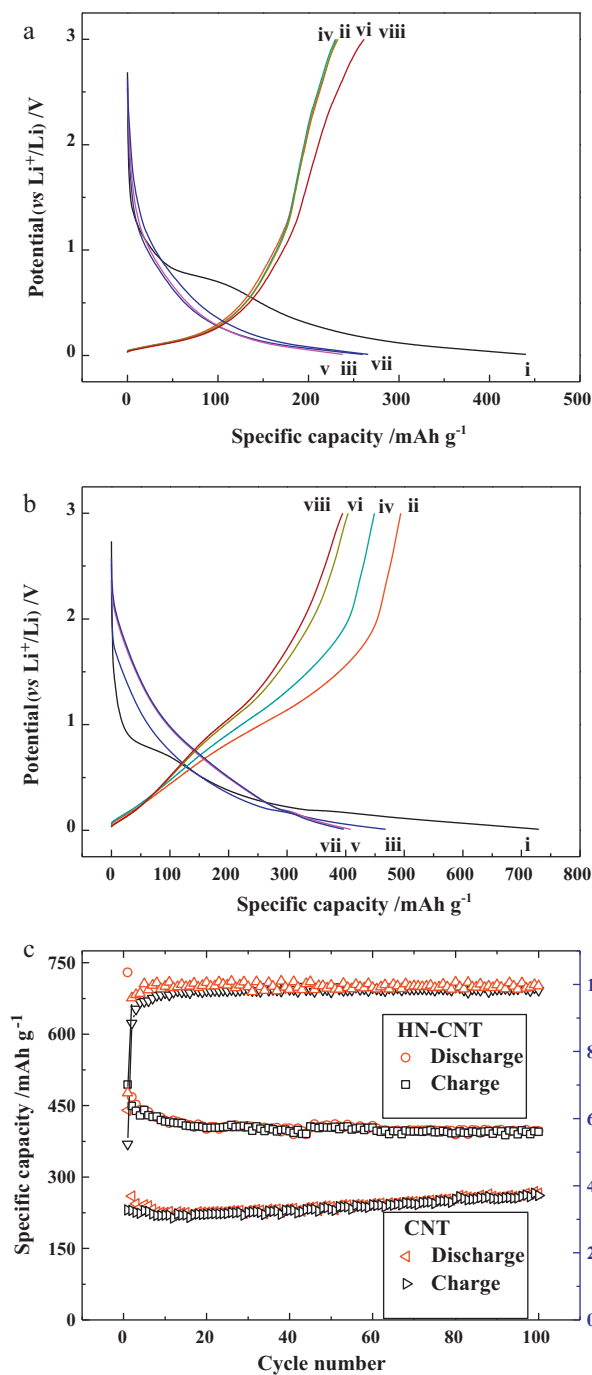
Fig. 6. Charge/discharge profiles of (a) CNTs and (b) HN-CNTs at a current density of 100 mA g^{-1}: (i) the first discharge, (ii) the first charge, (iii) the second discharge, (iv) the second charge, (v) the 50th discharge, (vi) the 50th charge, (vii) the 100th discharge, (viii) the 100th charge; (c) reversible charge/discharge capacity verse cycle numbers of CNTs and HN-CNTs at a current density of 100 mA g^{-1}.

100 mA g^{-1} in the 1st, 2nd, 50th and 100th cycle, respectively. During the first discharge, the high capacities of 440 mAh g^{-1} and 730 mAh g^{-1} were observed for CNTs and HN-CNTs, respectively, while the reversible capacities (C_{re}) of 231 mAh g^{-1} and 494 mAh g^{-1} were observed from the first charge. XPS results indicate graphitic nitrogen substitution in the carbon nanotubes. The existence of graphitic nitrogen results in an increase of reversible capacity. The higher the nitrogen content, the higher charge capacity [32]. Furthermore, the pyridinic unit introduction causes some defects in HN-CNTs, increasing the specific capacity [38,46]. On the

other hand, the connections at the bamboo structure are weak and the open edges of the graphene layers are terminated on the surface of the tubes. These locations are beneficial to Li$^+$ storage in HN-CNT anodes [31]. Therefore, HN-CNTs perform a higher reversible capacity than CNTs. HN-CNTs also show a much higher coulombic efficiency in the first cycle, 68%, in comparison to 52% for CNTs. The first cycles of both electrodes exhibit high irreversible capacities (C_{irre}), which could be attributed to the electrolyte decomposition and the formation of the SEI layer on the surface of the anodes as shown in CV curves in Fig. 5. In the sequent cycles, the coulombic efficiencies of both CNTs and HN-CNTs undergo an obvious increase, which is backed up by the disappearance of the reduction peak at around 0.7 V after the first cycle in CV curves in Fig. 5 [47,48].

The Li$^+$ storage performance of CNT and HN-CNT anodes for LIBs was determined by the galvanostatic charge/discharge cycling. At a current density of 100 mA g^{-1} in a voltage window of 0.01–3.00 V, the Li$^+$ storage capacity vs. cycle number is shown in Fig. 6c. Obviously, while both anode electrodes present the good cyclability during charge/discharge process, HN-CNTs display higher specific discharge capacity of 397 mAh g^{-1} compared with 266 mAh g^{-1} of CNTs after 100 cycles. The charge/discharge speed in a lithium ion battery can strongly depends on how fast its electrons and Li$^+$ can move. The rate capability is an important parameter of LIBs for many applications such as HEVs, which requires the fast discharge/charge rate [49,50]. The rate capability of CNT and HN-CNT anodes at various current densities from 100 mA g^{-1} to 1300 mA g^{-1} in a voltage window of 0.01–3.00 V at ambient temperature was presented in Fig. 7a and b. HN-CNTs show the higher but steadier capacities than CNTs, even at the high current density of 1300 mA g^{-1}. For both electrodes, the charge/discharge capacities decrease with the increase of the current density. Li$^+$ diffusion coefficient inside CNTs and HN-CNTs is limited during the processes of Li$^+$ intercalation/de-intercalation. There should be a gradient of the Li$^+$ concentration in anodes during charge/discharge process. The potential of CNTs and HN-CNTs drops to the cut-off potential rapidly when anode surface completes the discharge, but the center of the anodes does not complete the discharge process [51,52], which causes the capacity loss at high current densities. The higher the current densities, the higher the capacity loss. If we compared the discharge capacity of the second cycle at various current densities, HN-CNT anode was found to sustain higher capacity retention at 300 mA g^{-1}, 600 mA g^{-1}, 900 mA g^{-1}, 1000 mA g^{-1}, 1150 mA g^{-1}, and 1300 mA g^{-1} relative to the capacity at 100 mA g^{-1} than that of CNT anode (Fig. 7c). Therefore, HN-CNT anode was demonstrated to show the better rate capability than CNTs as anode for LIBs.

3.5. Structure change of CNTs and HN-CNTs after charge/discharge cycles

The results in Figs. 6 and 7 indicate that HN-CNT anode shows a much higher reversible capacity and better rate capability in comparison to CNT anode. SEM images of CNTs and HN-CNTs before and after cycling are shown in Fig. 8. After 100 cycles, no obvious morphology change of CNTs and HN-CNTs was observed. In particular, the bamboo-like structure of HN-CNTs remains intact after the charge/discharge process. The intact morphology provides a convincing evidence of good cycle performance as anodes for LIBs. In order to obtain increased understanding on the Li$^+$ storage behavior of CNTs and HN-CNTs, Raman analysis was carried out for CNTs and HN-CNTs before and after 100 cycles. Raman spectra were employed to obtain information regarding the change of crystallinity for CNTs and HN-CNTs. The G band with E_{2g} symmetry is ascribed to ordered sp^2 carbon at around 1595 cm^{-1} and the D band with A_{1g} symmetry at about 1310 cm^{-1} is related to disordered carbon, edge defects, and other defects (sp^3 bonded carbon,
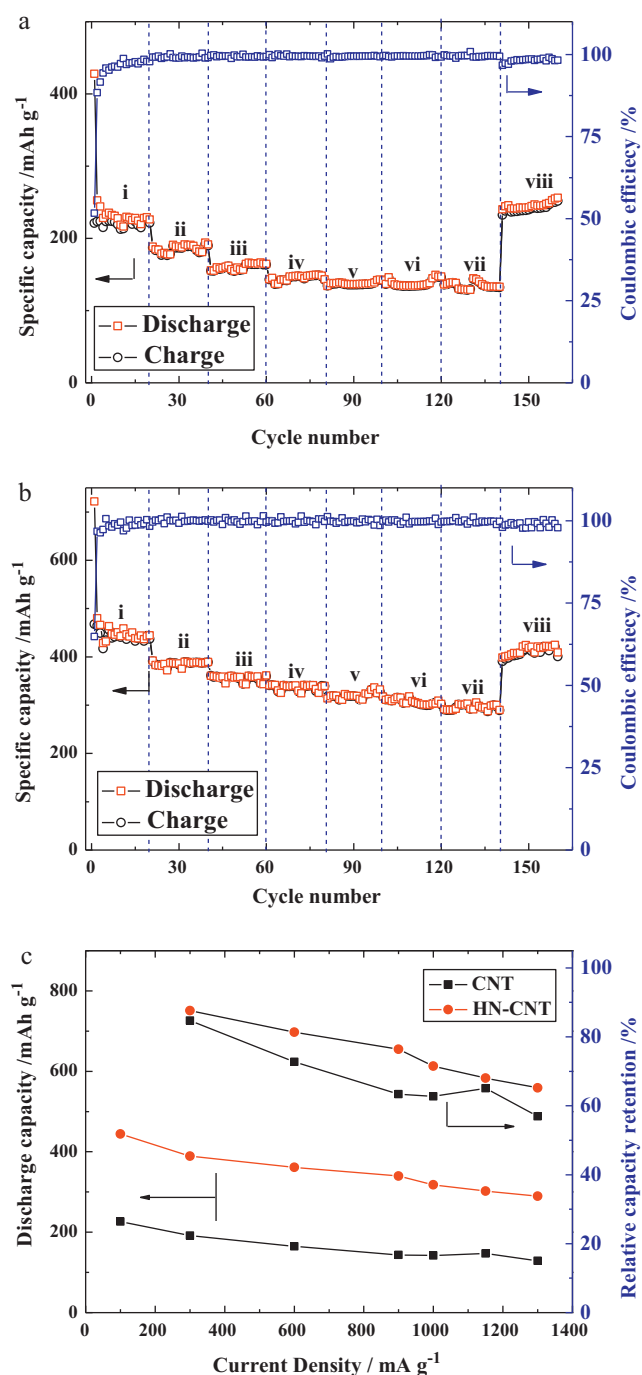

Fig. 7. Rate capability of (a) CNTs and (b) HN-CNTs at different current densities: (i) 100, (ii) 300, (iii) 600, (iv) 900, (v) 1000, (vi) 1150, (vii) 1300 and (viii) 100 mA g^{-1}; (c) discharge capacity of CNT and HN-CNT as a function of current density from 100 mA g^{-1} to 1300 mA g^{-1}.

dangling bonds, vacancies, and topological defects) [53]. As revealed in Raman in Fig. 9a and b, CNTs show D and G band at 1354 and 1579 cm^{-1}, respectively. After the nitrogen doping, the position of the G and D bands remain almost unchanged while the intensity of G band decreases too much. In Raman spectra, the integral intensity I_D and I_G is proportional to the number of the scattering disordered and ordered sp^2 bonding carbon atoms, respectively [54]. The I_D/I_G ratio can thus be used as a gauge to determine the degree of crystallinity of carbon. Deconvolution is a procedure for obtaining an essential spectrum from the original signal spectrum. After the deconvolution, Raman spectrum of CNTs and HN-CNTs
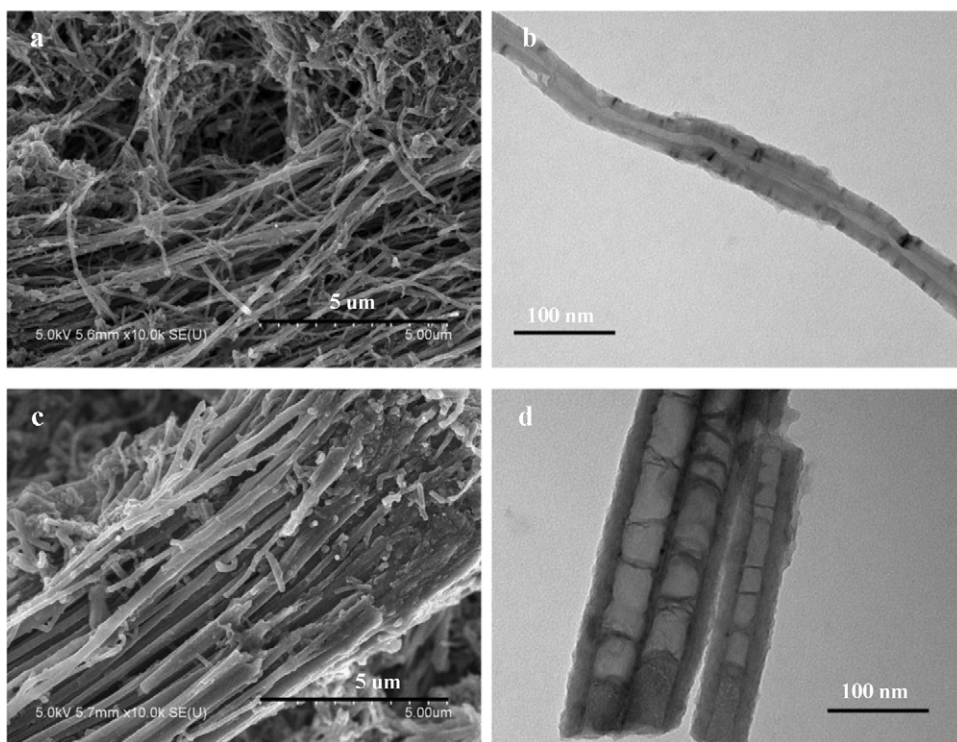
Fig. 8. Representative SEM and TEM images of (a and b) CNTs and (c and d) HN-CNTs after 100 charge/discharge cycles.
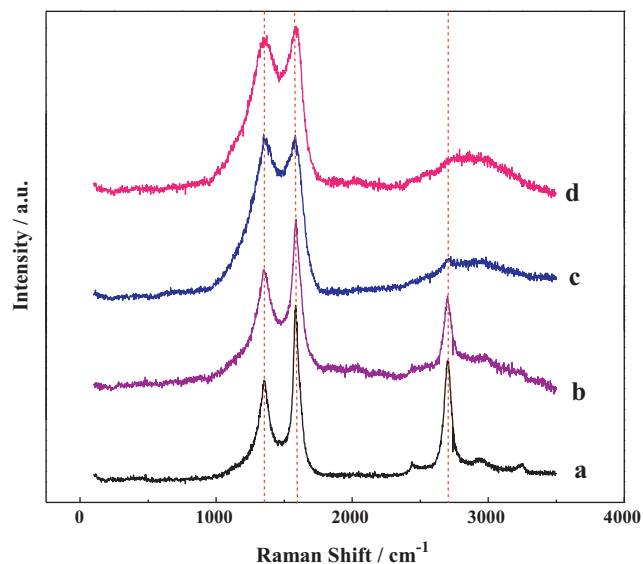
Fig. 9. Raman spectra of CNTs before (a)/after (b) 100 cycles and HN-CNTs before (c)/after (d) 100 cycles using 532.4 nm diode laser excitation at room temperature.

separately show G band and D band (see Fig. S1). It was calculated that I_D/I_G is 1.22 and 4.41 for CNTs and HN-CNTs, respectively. After the nitrogen introduction into the carbon nanotubes, the distinct increase in I_D/I_G suggested that some disordered carbon is presented in HN-CNTs, which indicates more defect sites for HN-CNTs. These defect sites provide more electrochemical active locations. Therefore, HN-CNTs show the higher specific capacity than CNTs. The Raman shift for both G-band and D-band did not show obvious move after Li^+ intercalation/de-intercalation into CNTs and HN-CNTs. For HN-CNTs, I_D/I_G slightly decreases from 4.41 to 3.78 before and after 100 cycles, while an increase from 1.22 to 1.91 for CNTs. Even after charge/discharge cycling, I_D/I_G of HN-CNTs is still much

higher than that of CNTs, as a consequent, HN-CNTs can deliver the higher specific capacity than CNTs in the 100th cycle.

4. Conclusions

HN-CNT anode for LIBs was systematically investigated in comparison to CNT anode. Our results demonstrated that HN-CNT anode shows much higher specific capacity of 494 mAh g^{-1} than CNTs, and still delivers the discharge capacity of 397 mAh g^{-1} in the 100th cycle (only 266 mAh g^{-1} for CNTs). Moreover, HN-CNTs display better rate capability than CNTs. The performance improvement is attributed to high concentration nitrogen (up to 16.4 at.%) into carbon nanotubes facilitating the higher electrical conductivity and the more defect sites in anodes which provide more Li^+ storage electrochemical active locations. Our study opens a new pathway for the use of HN-CNTs as anode material for LIBs.

Acknowledgments

Appendix A. Supplementary data

Supplementary data associated with this article can be found, in the online version, at doi:10.1016/j.jpowsour.2011.09.024.

References

[1] Y.S. Hu, R.D. Cakan, M.M. Titirici, J.O. Muller, R. Schlogl, M. Antonietti, J. Maier, Angew. Chem. Int. Ed. 47 (2008) 1645–1649.
[2] D. Derrien, J. Hassoun, S. Panero, B. Scrosati, Adv. Mater. 19 (2007) 2336–2340.

[3] B.J. Landi, M.J. Ganter, C.D. Cress, R.A. DiLeo, R.P. Raffaelle, Energy Environ. Sci. 2 (2009) 638–654.
[4] L.F. Cui, R. Ruffo, C.K. Chan, H.L. Peng, Y. Cui, Nano Lett. 9 (2009) 491–495.
[5] G.F. Ortiz, I. Hanzu, P. Lavela, P. Knauth, J.L. Tirado, T. Djeniziana, Chem. Mater. 22 (2010) 1926–1932.
[6] R. Teki, M.K. Datta, R. Krishnan, T.C. Parker, T.M. Lu, P.N. Kumta, N. Koratkar, Small 5 (2009) 2236–2242.
[7] Y. Yu, L. Gu, C.B. Zhu, P.A. Aken, J. Maier, J. Am. Chem. Soc. 131 (2009) 15984–15985.
[8] J. Zhang, Y.S. Hu, J.P. Tessonnier, G. Weinberg, J. Maier, R. Schlogl, D.S. Su, Adv. Mater. 20 (2008) 1450–1455.
[9] J. Hu, H. Li, X.J. Huang, Solid State Ionics 178 (2007) 265–271.
[10] E.J. Yoo, J. Kim, E. Hosono, H.S. Zhou, T. Kudo, I. Honma, Nano Lett. 8 (2008) 2277–2282.
[11] V. Subramanian, H.W. Zhu, B.Q. Wei, J. Phys. Chem. B 110 (2006) 7178–7183.
[12] H.J. Dai, Surf. Sci. 500 (2002) 218–241.
[13] D.S. Su, R. Schlogl, ChemSusChem 3 (2010) 136–168.
[14] K.P. Gong, F. Du, Z.H. Xia, M. Durstock, L.M. Dai, Science 323 (2009) 760–764.
[15] A. Thess, R. Lee, P. Nikolaev, H.J. Dai, P. Petit, J. Robert, C.H. Xu, Y.H. Lee, S.G. Kim, A.G. Rinzler, D.T. Colbert, G.E. Scuseria, D. Tomanek, J.E. Fischer, R.E. Smalley, Science 273 (1996) 483–487.
[16] M.M.J. Treacy, T.W. Ebbesen, J.M. Gibso, Nature 381 (1996) 678–680.
[17] R.H. Baughman, A.A. Zakhidov, D.H. WA, Science 297 (2002) 787–792.
[18] H. Shimoda, B. Gao, X.P. Tang, A. Kleinhammes, L. Fleming, Y. Wu, O. Zhou, Phys. Rev. Lett. 88 (2001), 015502-1-015502-4.
[19] V. Meunier, J. Kephart, C. Roland, J. Bernholc, Phys. Rev. Lett. 88 (2002), 075506-1-075506-4.
[20] J. Zhao, A. Buldum, J. Han, J.P. Lu, Phys. Rev. Lett. 85 (2000) 1706–1709.
[21] Y.J. Xu, X. Liu, G.L. Cui, B. Zhu, G. Weinberg, R. Schlogl, J. Maier, D.S. Su, ChemSusChem 3 (2010) 343–349.
[22] H. Zhang, G.P. Cao, Z.Y. Wang, Y.S. Yang, Z.J. Shi, Z.N. Gu, Electrochim. Acta 55 (2010) 2873–2877.
[23] B.J. Landi, M.J. Ganter, C.M. Schauerman, C.D. Cress, R.P. Raffaelle, J. Phys. Chem. C 112 (2008) 7509–7915.
[24] J.Y. Eom, D.Y. Kim, H.S. Kwon, J. Power Sources 157 (2006) 507–514.
[25] S.H. Ng, J. Wang, Z.P. Guo, J. Chen, G.X. Wang, H.K. Liu, Electrochim. Acta 51 (2005) 23–28.
[26] R.A. Dileo, A. Castiglia, M.J. Ganter, R.E. Rogers, C.D. Cress, R.P. Raffaelle, B.J. Landi, ACS Nano 4 (2010) 6121–6131.
[27] I. Lahiri, S.W. Oh, J.Y. Hwang, S. Cho, Y.K. Sun, R. Banerjee, W. Choi, ACS Nano 4 (2010) 3440–3446.
[28] R.S. Lee, H.J. Kim, J.E. Fischer, A. Thess, R.E. Smalley, Nature 388 (1997) 255–257.
[29] A.M. Rao, P.C. Eklund, S. Bandow, A. Thess, R.E. Smalley, Nature 388 (1997) 257–259.
[30] M. Terrones, P.H. Redlich, N. Crobert, S. Trazobares, W.K. Hsu, H. Terrones, Y.Q. Zhu, J.P. Hare, C.L. Reeves, A.K. Cheetham, M. Rühle, H.W. Kroto, D.R.M. Walton, Adv. Mater. 11 (1999) 655–658.
[31] D.Y. Zhang, G.Y. Zhang, S. Liu, E.G. Wang, Q. Wang, H. Li, X.J. Huang, Appl. Phys. Lett. 79 (2001) 3500–3502.
[32] Y.P. Wu, S.B. Fang, Y.Y. Jiang, Solid State Ionics 120 (1999) 117–123.
[33] H. Liu, D. Arato, R.Y. Li, Y. Zhang, P. Merel, X.L. Sun, Surf. Coat. Technol. 202 (2008) 4114–4120.
[34] H. Liu, Y. Zhang, R.Y. Li, X.L. Sun, S. Desilets, H. Abou-Rachid, M. Jaidann, L.S. Lussier, Carbon 48 (2010) 1498–1507.
[35] Y. Zhong, M. Jaidann, Y. Zhang, G.X. Zhang, H. Liu, R.Y. Li, X.L. Sun, H. Abou-Rachid, L.S. Lussier, J. Phys. Chem. Solids 71 (2010) 134–139.
[36] J. Liu, Y. Zhang, M.I. Ionescu, R.Y. Li, X.L. Sun, Appl. Surf. Sci. 257 (2011) 7837–7844.
[37] G. Kaushik, K. Mukul, M. Takahiro, A. Yoshinori, J. Mater. Chem. 20 (2010) 4128–4134.
[38] G. Kaushik, K. Mukul, M. Takahiro, A. Yoshinori, Carbon 48 (2010) 191–200.
[39] S. Lim, S. Yoon, I. Mochida, D. Jung, Langmuir 25 (2009) 8268–8273.
[40] C.V. Rao, C.R. Cabrera, Y. Ishikawa, J. Phys. Chem. Lett. 1 (2010) 2622–2627.
[41] Y. Fang, D. Gu, Y. Zou, Z.X. Wu, F.Y. Li, R.C. Che, Y.H. Deng, B. Tu, D.Y. Zhao, Angew. Chem. Int. Ed. 49 (2010) 7987–7991.
[42] M. Terrones, P.M. Ajayan, F. Banhart, X. Blase, D.L. Carroll, J.C. Charlier, R. Czerw, B. Foley, N. Grobert, R. Kamalakaran, P. Kohler-Redlich, M. Rühle, Appl. Phys. A 74 (2002) 355–361.
[43] G. Liu, H. Zheng, A.S. Simens, A.M. Minor, X. Song, V.S. Battaglia, J. Electrochem. Soc. 154 (2007) A1129–A1134.
[44] H.J. Kim, J.M. Kim, W.S. Kim, H.J. Koo, D.S. Bae, H.S. Kim, J. Alloys Compd. 509 (2011) 5662–5666.
[45] N.H. Idris, M.M. Rahman, J.Z. Wang, Z.X. Chen, H.K. Liu, Compos. Sci. Technol. 71 (2011) 343–349.
[46] S. Jalili, R. Vaziri, Mol. Phys. 109 (2011) 687–694.
[47] J.R. Dahn, T. Zheng, Y. Liu, J.S. Xue, Science 270 (1995) 590–593.
[48] M. Winter, O.J. Besenhard, M.E. Spahr, P. Novak, Adv. Mater. 10 (1998) 725–763.
[49] K. Kang, Y.S. Meng, J. Breger, C.P. Grey, G. Ceder, Science 311 (2006) 977–980.
[50] B. Kang, G. Ceder, Nature 458 (2009) 190–193.
[51] K. Dokko, N. Nakata, K. Kanamura, J. Power Sources 189 (2009) 783–785.
[52] H. Buqa, D. Goers, M. Holzapfel, M.E. Spahr, P. Novak, J. Electrochem. Soc. 152 (2005) A474–A481.
[53] D.Y. Pan, S. Wang, B. Zhao, M.H. Wu, H.J. Zhang, Y. Wang, Z. Jiao, Chem. Mater. 21 (2009) 3136–3142.
[54] I. Gert, D.R. Annett, Adv. Eng. Mater. 7 (2005) 694–705.